Intermodel Spread of Historical Indian Monsoon Rainfall Change in CMIP6: The Role of the Tropical Pacific Mean State

Marcellin Guilbert, Pascal Terray, Juliette Mignot

Intermodel Spread of Historical Indian Monsoon Rainfall Change in CMIP6: The Role of the Tropical Pacific Mean State

MARCELLIN GUILBERT,[a] PASCAL TERRAY,[a] AND JULIETTE MIGNOT[a]

[a] *Laboratoire d'Océanographie et du Climat: Expérimentations et Approches Numériques, Institut Pierre-Simon Laplace, Sorbonne Université/CNRS/IRD/MNHN, Paris, France*

(Manuscript received 3 August 2022, in final form 15 February 2023, accepted 21 February 2023)

ABSTRACT: Robust projections of the Indian summer monsoon rainfall (ISMR) are critical as it provides 80% of the annual precipitation to more than 1 billion people who are very vulnerable to climate change. However, even over the historical period, state-of-the-art climate models have difficulties in reproducing the observed ISMR trends and are affected by a large intermodel spread, which questions the reliability of ISMR projections. Such uncertainty could come from internal variability or model biases. Here, we study the impact of the latter on the historical forced change of ISMR in 34 models from CMIP6. First, we show that models' biases over India do not significantly impact how they simulate the historical change of ISMR. However, we do find statistically significant relationships between ISMR historical forced changes and remote rainfall and temperature biases within the tropics by using a maximum covariance analysis (MCA). Our results highlight the key role of tropical Pacific sea surface temperature (SST) mean state biases as an important source of intermodel spread in the ISMR change. The physical mechanisms underlying these statistical relationships between ISMR change and the intermodel spread of Pacific SST biases are finally explored. We found that models having El Niño/La Niña–like mean SST bias in the Pacific tend to exhibit El Niño/La Niña–like changes over the historical period, impacting ISMR through a shift in the Walker circulation and Rossby wave propagation across the Pacific.

KEYWORDS: Monsoons; Climate change; ENSO

1. Introduction

Indian summer monsoon rainfall (ISMR) plays a critical role for India as it provides up to 80% of the annual precipitation from June to September (Ramage 1971; Jain and Kumar 2012) in a country that represents about 20% of today's world population. ISMR changes have profound impacts on local livelihood, economic development, and social stability. As an illustration, in 2002, India suffered an unusually weak summer monsoon with a 20% ISMR decrease. This resulted in billions of dollars in economic damages (Gadgil et al. 2004) and affected more than a billion people through drinking and sanitation. In this context, the weakening trend of the Indian summer monsoon at the end of the twentieth century and its possible recovery during the last 20 years are of great concern for India (Raghavan et al. 2016; Jin and Wang 2017).

Consequently, predicting ISMR evolution is critically important for India, and the Indian government launched the "Monsoon Mission" in 2012, a national initiative which aims to tackle scientific and economic challenges raised by the predictability and future of the Indian monsoon (Rao et al. 2019). One of the major achievements of this ongoing project is that an Indian coupled model [Indian Institute of Technology Madras Earth System Model, version 2 (IITM-ESMv2)] contributed to phase 6 of the Coupled Model Intercomparison Project (CMIP6) (Swapna et al. 2018). More generally, the will to better understand monsoon variability at different time scales is illustrated by the coordination of a monsoon-dedicated international cooperation program in CMIP6 called the Global Monsoon Model Intercomparison Project (Zhou et al. 2016).

Understanding the unfolding challenges of the future ISMR evolution relies on coupled atmosphere–ocean general circulation models (CGCMs) and climate projections. However, even over the historical period, large uncertainties remain about the ability of CGCMs to reproduce ISMR seasonal cycles and trends (Saha et al. 2014; Annamalai et al. 2017). To improve the reliability of CGCMs, it is necessary to identify the factors that are responsible for their inaccuracy in reproducing the evolution of the ISMR over the historical period and to distinguish between the part of this failure that is related to systematic errors and other factors such as internal variability.

In terms of radiative forcing, the first main anthropogenic forcing is the increase of atmospheric GHGs. The thermodynamic effect of GHGs on precipitation refers to the increase of precipitable water in the atmosphere induced by the increase in temperature. This implies that moisture convergence must increase in response to global warming if one assumes unchanged atmospheric circulation. This is called the "wet-get-wetter" mechanism (Vecchi and Soden 2007). The impact of GHG forcing on circulation is also of critical importance. In recent decades, the Indian subcontinent has warmed faster than the Indian Ocean (IO), thereby reinforcing the meridional thermal gradient

Denotes content that is immediately available upon publication as open access.

Supplemental information related to this paper is available at the Journals Online website: https://doi.org/10.1175/JCLI-D-22-0585.s1.

Corresponding author: Marcellin Guilbert, marcellin.guilbert@locean.ipsl.fr

DOI: 10.1175/JCLI-D-22-0585.1

in the lower troposphere, which enhances ISMR (Lau and Kim 2017; Singh et al. 2019; Jin et al. 2020). However, reducing GHGs' impact over ISMR to surface temperature gradient would be erroneous (Ma and Yu 2014; Lau and Kim 2017). Indeed, latent heating also modulates the land–ocean thermal contrast and the monsoon circulation in the mid–upper troposphere according to the thermal wind relationship (Dai et al. 2013). This overview illustrates the complexity of ISMR response to GHG forcing and possible sources of uncertainty in the way models represent the evolution of ISMR.

The second main anthropogenic forcing is the increase of atmospheric aerosols, which have on average a cooling effect at the surface (Ming et al. 2011). Aerosol emission rose sharply during the 1950s in the Northern Hemisphere, leading to an asymmetric cooling at the end of the twentieth century. This cooling may have caused a reduction in the summer interhemispheric energy imbalance resulting in an equatorward shift of the intertropical convergence zone (ITCZ) and hence of ISMR (Salzmann et al. 2014; Polson et al. 2014). At the regional scale, aerosols have furthermore compensated for GHG-induced temperature increases over South Asia, but not over the IO (Lau and Kim 2017; Li et al. 2018; Singh et al. 2019; Seth et al. 2019), leading to a reduced land–sea thermal contrast, which has contributed to slowing down the monsoon circulation and led to a decrease in precipitation during the twentieth century (Li et al. 2015). Even if the direct effect is dominant, the indirect effect of aerosols, which refers to changes induced in clouds' radiative properties, their frequency, and their lifetimes, should not be overlooked. Indeed, CGCMs including both processes tend to reproduce better temperature and precipitation records over the twentieth century (Wilcox et al. 2013; Wang et al. 2015).

In addition to uncertainty coming from these complex processes, the recent ISMR changes in models may also be significantly influenced by internal variability (Huang et al. 2020). The interdecadal variability of the IO SST, which refers to a basinwide warm (cold) phase, is linked to ISMR through increased (decreased) southwesterly winds (Vibhute et al. 2020). The interdecadal Pacific oscillation (IPO), which is characterized by a tropical Pacific warmer or colder than average, also has remote impacts on ISMR variations (Chinta et al. 2022). The positive IPO phase weakens the Walker and Hadley circulations, which results in decreased ISMR (Joshi and Kucharski 2017). A transition from a cold to a warm phase of the IPO is thus another factor that may have contributed to the drying trend of ISMR over the last half of the twentieth century (Salzmann and Cherian 2015; Huang et al. 2020).

The relative roles of these different factors may not be stationary in time, both in the observations and CGCMs, and they may be altered in the latter due to systematic errors in simulating Indian summer monsoon (ISM) (Hurley and Boos 2013; Annamalai et al. 2017; Terray et al. 2018) or because of missing key physical processes, for example, those related to clouds (Oueslati et al. 2016). As noted by Oueslati et al. (2016), present-day climatological biases in specific humidity and profile of vertical velocity are important sources of intermodel spread in the tropics, both over land and ocean, in CMIP5 models. The parameterizations of convection or orography are also sources of uncertainty to reproduce ISMR and its long-term trend (Hurley and Boos 2013; Sabeerali et al. 2015). Continental errors, including large cold biases over Eurasia and the subtropical deserts adjacent to India, can also affect ISMR and its long-term behavior by modulating the ISM circulation and the fast ISM response to GHG forcing (Endo et al. 2018; Terray et al. 2018; Sooraj et al. 2019). Biases in adjacent or remote regions can also impact ISMR. As an illustration, errors in the SST climatology of the eastern equatorial IO have been shown to be linked to errors in ISM simulation through Bjerknes feedback (Annamalai et al. 2017), and cold SST biases in the Arabian Sea can weaken humidity transport toward India (Levine et al. 2013). Beyond climatological errors, biases in simulated modes of interannual variability, like El Niño–Southern Oscillation (ENSO) or the Indian Ocean dipole (IOD), can also induce errors in ISMR projections (Li et al. 2017).

The skill of CGCMs at reproducing ISM climatology has increased from CMIP3 to CMIP6 (Rajendran et al. 2022; Choudhury et al. 2022). However, most current CGCMs still exhibit a large and persistent dry ISMR bias and a strong intermodel spread for ISMR projections (Sperber et al. 2013; Jain et al. 2019; Jin et al. 2020; Katzenberger et al. 2021). It is thus necessary to reduce models' uncertainties so as to strengthen our confidence in the models' projections. The main goal of this study is to provide a systematic assessment of the statistical and physical relationships between intermodel spread of ISMR changes and models' biases. A few previous studies have already discussed some aspects of these relationships but have been restricted to the possible influence of one basin or region and using CMIP5 future projections (Li et al. 2017; Shamal and Sanjay 2021). Here, we focus on the influence of precipitation and surface temperature biases over the whole tropical band on the historical changes of ISMR in the new CMIP6 database. We choose to focus on the historical period in order to take advantage of the larger number of models, each of them including more members than over the future period. The underlying questions are as follows: 1) Is there a local link between climatological biases over India and ISMR change? 2) Are there links with some remote biases over land or the tropical oceanic basins? 3) By which physical processes do local and/or remote biases influence ISMR historical evolution? Section 2 describes observational data, model simulations, and analysis methods used in this study. In section 3, we evaluate historical simulations against observations and investigate local relationships. Section 4 extends the scope of section 3 to assess relationships with remote biases over the whole tropics with the help of maximum covariance analysis (MCA). The last section presents a summary and future perspectives.

2. Data and methods

a. *Coupled simulations and validation datasets*

This study is based on the outputs of 34 CGCMs from CMIP6 (see supplemental Table S1 in the online supplemental material; Eyring et al. 2016). Most models have multiple members of the "historical" experiment (herein referred to as "historical,"

TABLE 1. Definition of the indices used in the present study. Angle brackets $\langle\cdot\rangle$ stand for spatial averaging; the superscript indicates the surface type or the atmospheric level over which the average is taken, when relevant, and the subscript the domain.

Indices	Domain and variable used
ISMR	$\langle \mathrm{Pr} \rangle^{\mathrm{Land}}_{[7°\mathrm{N};30°\mathrm{N}],[65°\mathrm{E};95°\mathrm{E}]}$
Precipitable water content over India (PRWI)	$\langle \mathrm{PRW} \rangle^{\mathrm{Land}}_{[7°\mathrm{N};30°\mathrm{N}],[65°\mathrm{E};95°\mathrm{E}]}$
Webster–Yang index (WYI)	$\langle U \rangle^{850\mathrm{hPa}}_{[0°\mathrm{N};20°\mathrm{N}],[40°\mathrm{E};110°\mathrm{E}]} - \langle U \rangle^{200\mathrm{hPa}}_{[0°\mathrm{N};20°\mathrm{N}],[40°\mathrm{E};110°\mathrm{E}]}$
Monsoon meridional circulation index (MMCI)	$\langle V \rangle^{850\mathrm{hPa}}_{[10°\mathrm{N};30°\mathrm{N}],[70°\mathrm{E};110°\mathrm{E}]} - \langle V \rangle^{200\mathrm{hPa}}_{[10°\mathrm{N};30°\mathrm{N}],[70°\mathrm{E};110°\mathrm{E}]}$
Eurasian land–ocean thermal contrast (ELOTC)	$\langle \mathrm{Tas} \rangle^{\mathrm{Land}}_{[0°\mathrm{N};60°\mathrm{N}],[30°\mathrm{E};180°]} - \langle \mathrm{Tas} \rangle^{\mathrm{Ocean}}_{[10°\mathrm{S}\,60°\mathrm{N}],[30°\mathrm{E};180°]}$
Pacific equatorial SST gradient	$\langle \mathrm{SST} \rangle_{[5°\mathrm{S};5°\mathrm{N}],[130°\mathrm{E};170°\mathrm{W}]} - \langle \mathrm{SST} \rangle_{[5°\mathrm{S};5°\mathrm{N}],[80°\mathrm{W};140°\mathrm{W}]}$

covering the period from 1850 to 2014). All these historical integrations are forced by the same time-varying external radiative forcings (both natural and anthropogenic) derived from observations, but they have different initial conditions. The monthly mean outputs used in our analysis include rainfall (Pr), precipitable water (PRW), surface temperature (Ts), near-surface air temperature (Tas), sea level pressure (SLP), and horizontal winds (U and V) at different levels.

For model validation of the precipitation field, we use the Global Precipitation Climatology Project (GPCP) monthly mean precipitation flux dataset from 1979 to 2017 (Adler et al. 2003). For surface temperature, precipitable water, and horizontal winds we use ERA-Interim (Dee et al. 2011). We also use the all-India rainfall (AIR) index, which is an area-weighted mean from a fixed ensemble of 306 rain gauge stations over India (Parthasarathy et al. 1994), and an ISMR index derived from the India Meteorological Department (IMD) rainfall dataset to monitor the observed ISMR evolution over the historical period. This last index is based on about 6329 stations (with least 90% data availability over the period) for the period 1901–2013 (Mohapatra et al. 2018).

b. Climate and ISMR indices

To understand how models' biases interact with the change of ISM rainfall and circulation, we define several indices, which serve as proxies for the main thermodynamic and dynamic components of the moisture budget (Seager et al. 2010). The different climate and dynamical indices used in this study are defined in Table 1. The overall thermodynamic change is approximated by averaging the change of the PRW change over the domain. It corresponds to the evolution of humidity integrated over the whole atmospheric column. The dynamical changes are split into zonal and meridional contributions by using the Webster–Yang index (WYI) and the monsoon meridional circulation index (MMCI), respectively (Webster and Yang 1992; Goswami et al. 1999). These indices are measures of the vertical shear of zonal and meridional winds between the 850- and 200-hPa levels, respectively. These shears are well related to the strength of the monsoon circulation and to tropospheric temperature gradients (Dai et al. 2013). Finally, we use the difference of surface temperature between part of the Eurasian continent and the surrounding oceans, later referred to as Eurasian land–ocean thermal contrast (ELOTC), to determine whether or not the large-scale surface thermal contrast is a key factor in shaping the ISM change during the historical period, as it is in projections (Jin et al. 2020). Note that thereafter, "ISMR change" refers to regionally averaged ISM rainfall (defined above as ISMR) change over the historical period (see Table 1), while ISM rainfall change refers to change in the rainfall pattern over India over the historical period. The former is an index, while the latter is a spatial pattern.

c. Methods

We define climate change over the historical period as the difference of climatological means between the end of the historical period (1979–2014) and the early industrial period (1850–75). This definition will be justified in section 3a in which we demonstrate that ISMR changes are most prominent during the last decades of the historical period. Model biases are defined as the differences between model and validation data climatologies over the 1979–2014 period during which the quality of observations and reanalysis products has greatly improved as compared to the early period. Model variability is defined as the average over the various available members of the temporal standard deviation computed over 1979–2014. Among the available datasets, we choose GPCP (ERA-Interim) to define precipitation (temperature) biases, while AIR and IMD are used to evaluate ISMR trends over the historical period. Our analysis will focus on June–September (JJAS) as it is the monsoon season and all datasets were interpolated onto a common 2.8° × 2.8° horizontal resolution by bilinear interpolation prior to the analysis. It should be noted that due to the specific focus on JJAS season, the time-lagged links between ISM changes and biases are not explored in this study. However, our results are robust if annual rather than JJAS averages are considered for the tropical SST and rainfall biases in the analysis.

For both observations and simulations, velocity potential, streamfunction, and divergent and rotational winds were calculated at different levels from horizontal winds with the spectral method (Tanaka et al. 2004). Furthermore, in order to accurately describe the low-frequency variations in the observed and simulated ISMR time series in Fig. 1, a locally weighted regression called locally estimated scatterplot smoothing (LOESS; Cleveland and Devlin 1988) was applied to the ISMR index (only for this time series). LOESS is a nonparametric method for fitting a smoothed regression curve to data through local

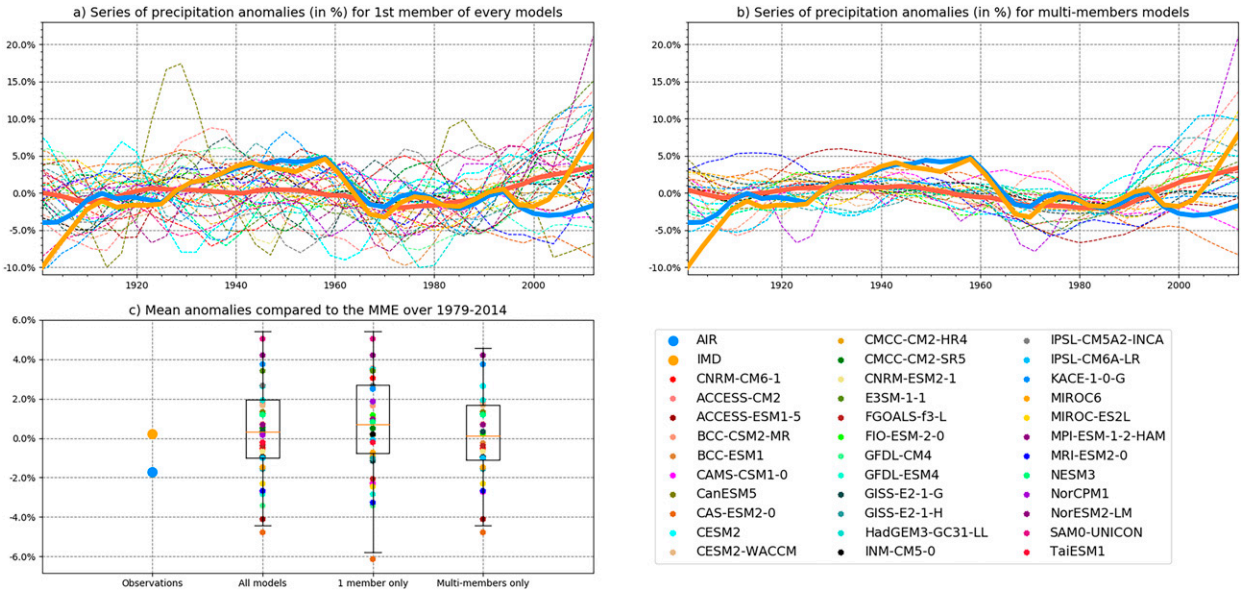

FIG. 1. (a) Low-pass-filtered ISMR time series represented as normalized anomalies and expressed in percent of the respective mean over 1901–2012 for each time series. The thin lines represent the first historical member of each of the 34 models available from the CMIP6 repository (see supplemental Table S2), while bold lines represent the MMM of these 34 first historical members (red) and the observed AIR (blue) and IMD (orange) indices, respectively. (b) As in (a), but where thin lines represent the multimember average for all models with more than one member (25 of 34 models; see supplemental Table S1 for details), and MMM is calculated on these multimembers only. (c) Mean anomalies over the 1979–2014 period relative to 1901–2012. The first column is for observations, with the same color code as in (a) and (b). The last three columns are whisker plots for three different ensembles of simulations. The first whisker column is for the multimember average for all the 34 available models, even those with only one member available. The second whisker column considers only the first member for each model [see (a)]. The third whisker column considers the multimember average for the 25 models with more than one member available [see (b)]. In all panels, the observed and simulated ISMR raw time series have been low-pass filtered with LOESS (Cleveland and Devlin 1988). See text and section 2 for details.

smoothing. We applied LOESS with a moving time window of 20 years (equivalent to a low-pass filter eliminating fluctuations with periodicities less than 20 years) to the full time series, and we chose to show the low-pass-filtered time series on the period 1901–2012, which is the common period for the observations and the simulations. The ISMR climatology over this period was then calculated for each dataset in order to express the smoothed time series as anomalies (in percentages) with respect to this climatology. Note that all other computations use the raw data without any filtering.

To investigate the first-order linear relationships between changes over the historical period and model biases as seen from climate indices, we use scatterplots and regressions. For a more systematic exploration, we use MCA, which extracts the dominant covariability patterns from two geophysical datasets (Bretherton et al. 1992; Cherry 1997). MCA calculation is described in detail in supplemental Text S1.

3. ISMR trends, tropical biases, and changes over the historical period

a. *ISMR trends over the historical period*

First, we document the skill of CMIP6 models in simulating the ISMR modulations over the historical period. It has been demonstrated that CMIP5 models were not skillful in this respect (Saha et al. 2014). AIR and IMD are used for observations, as they cover the whole twentieth century, and the ISMR index as defined in Table 1 is used for simulations.

AIR and IMD oscillate mainly between −5% and 5% between 1900 and 2012, except at the beginning and end of this period when variations are stronger (Fig. 1a; see the thick blue and orange lines). The correlation between AIR and IMD is significant ($r = 0.70$; $p < 0.01$), which proves an overall good agreement between our validation datasets. However, even if both observation datasets show an increase of ISMR over the recent period (2000–12; Jin and Wang 2017), there is a surprising disagreement on the magnitude of this wetting trend. This difference could possibly be related to the variable network of stations used in IMD or a too-coarse network in AIR (Lin and Huybers 2019; Singh et al. 2019). This highlights strong uncertainty on the observed recent ISMR trend and potential problems in the validation datasets.

This recent recovery of the monsoon has been attributed to an increase in atmospheric moisture content coupled to a favorable land–sea thermal contrast between East Asia and the western North Pacific Ocean (Huang et al. 2020; Rajendran et al. 2022) and between the Indian subcontinent and the IO (Jin and Wang 2017; Roxy 2017). Such evolution may also arise from the sustained increase of GHG emissions. Recent studies furthermore showed that, as sulfate aerosol mitigation policies are now applied, GHG forcing is overtaking the aerosol forcing

after the 1980s (Seth et al. 2019; Allan et al. 2020). If GHGs are responsible for the recent wetting ISMR trend, the latter is likely to become more prominent in the future (Katzenberger et al. 2021).

Figure 1a also shows the first (single for models proposing only one member; see supplemental Table S2) member of historical realizations taken from all the 34 CMIP6 models available from the Earth System Grid Federation repository. Taken as a whole, this ensemble of simulations yields relatively large multidecadal variations of ISMR with an amplitude generally comparable to those found in observations (Fig. 1a). The multimodel ensemble mean (MMM) (thick red line) typically yields weaker variations than the validation datasets (from −2% to +4%), which is expected as simulated internal variability is damped by the model averaging. The relative amplitude of the drying ISMR trend during the 1950–90 period seen in both AIR and IMD (Bollasina et al. 2011; Saha et al. 2014; Salzmann et al. 2014; Roxy et al. 2015) is not well reproduced by the MMM, as in CMIP5. This result is consistent with the partial attribution of this drying trend to internal variability (Huang et al. 2020). After the 2000s, the MMM increases and peaks around +4%, which is comparable to the observed ISMR interannual variability (which is typically about 10% of the ISMR mean).

This recent recovery of ISM thus appears consistently in the MMM (computed from single or first member for each model), IMD, and AIR (Fig. 1a). This is in line with the partial attribution of this wetting trend to external forcings. However, consistent with the weaker amplitude, the slope of MMM recent trend is much weaker than the observed one. Furthermore, the single-member intermodel spread increased from the 1980s until the end of the period. Indeed, in single realizations, the anomalies are spanning from −8% to +21% toward the end of the period, while they were earlier approximately ranging between −7% and +6%.

Since the single members are influenced both by natural variability and external forcings, it is difficult to distinguish their respective contributions to the increase in the intermodel spread. To get further insights about the origin of this increase, Fig. 1b presents the temporal evolution of ISMR in multimember average for all models with more than one member (25 of 34 models). The multidecadal variability of ISMR modeled over the twentieth century is largely reduced in these multimember ensembles as expected from the averaging which damps the internal variability. The MMM is nevertheless very close to the one computed from single-member only for the whole period ($r = 0.93$), including the recent wetting period. Interestingly, the increase in the intermodel spread is still present in the multimember averages. This suggests that this spread is also associated with a biased and variable response of the models to external forcings.

To validate more quantitatively this hypothesis, we now focus on the distributions of the mean averages over the 1979–2014 period for the single-member versus multimember model sets as these time averages are used to define the climate changes (see section 2 for details) in the following sections. The two right-hand columns in Fig. 1c show that, when averaged over the 1979–2014 period, the spread of ISMR change as represented in the CMIP6 database is slightly weaker when considering only the 25 models offering multiple members of historical simulations than when considering all the 34 single or first historical realizations. Nevertheless, a two-sample version of the Smirnov–Kolmogorov test (Hodges 1958) applied to the two empirical distributions leads to the rejection of the hypothesis that these two distributions differ even at a very low confidence level (p value is 0.80).

Taking into account this result and in order to keep the model panel as large as possible to maximize the significance of our results, we consider in the following the multimember average for each of our 34 models even when only one member is available without any weighting (second column of Fig. 1c). Figure 1c illustrates that this ensemble only shows small differences with the two other ones. By using a Smirnov–Kolmogorov test as above, we could furthermore show that all these distributions are similar ($p > 0.80$). This allows us to use a multimember average for all of our models despite the fact that some of them have only one member, because the time average over the last 35 years is sufficient to damp the effect of internal variability in all cases. This also justifies our choice to give the same weight to each of the models in the rest of the study, regardless of their number of members. Finally, in order to have an overview of the relative importance of this intermodel spread with respect to internal variability, we have assessed the intramodel spread (related to internal variability) for CMIP6 models with more than one member (see supplemental Fig. S3). Interestingly, for the majority of models, the intramodel spread is lower than the intermodel spread, with the exception of the CanESM5 model.

b. *Contributions to ISMR change and spread*

To gain more insights into the physical mechanisms underlying the ISMR changes over the historical period and its intermodel spread, we now study its links with dynamical or large-scale indices (see section 2 and Table 1).

MMMs of WYI (Fig. 2a) and MMCI (Fig. 2d) changes averaged over the multimodel ensemble described above show a decrease over the historical period (see the crosses in the panels), while MMM of precipitable water content over India (PRWI) change shows a strong increase (Fig. 2e). This indicates that the small decrease in the MMM of ISMR seen in the y axis of each panel in Fig. 2 is due to a decrease in the dynamic component, which is partially compensated by the thermodynamic component. This may explain why, even if global warming and ISMR are both significantly correlated with the change in PRWI, they are not correlated with each other (Fig. 2b; $r = 0.25$; $p > 0.10$). On the other hand, the intermodel spread of PRWI is significantly correlated with the global surface temperature change among models ($r = 0.50$; $p < 0.01$; not shown), illustrating the link between thermodynamics of ISMR and global warming in agreement with the Clausius–Clapeyron relationship. Consistently, there is also a significant relationship between the intermodel spread of ISMR and PRWI changes (Fig. 2e).

The intermodel spread is also significantly related to dynamical changes with a very strong relationship between the ISMR and MMCI changes (Fig. 2d) and a weaker, but still

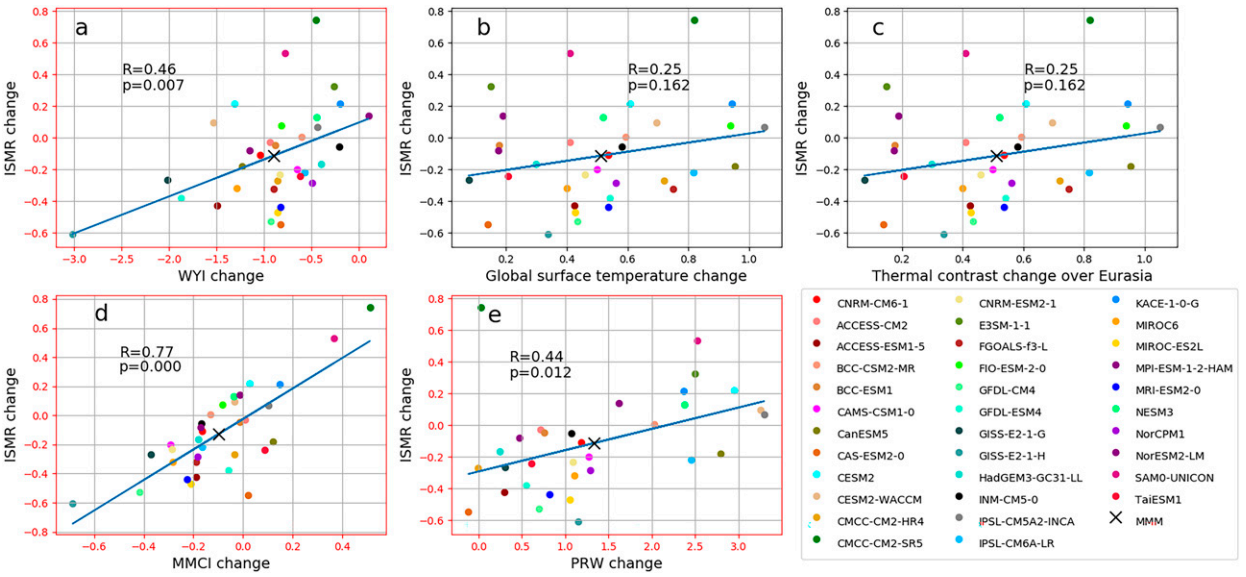

FIG. 2. Scatterplots of ISMR change (mm day^{-1}; defined in section 2 as the difference of JJAS means between 1979–2014 and 1850–1875), respectively, with changes of (a) the WYI (m s^{-1}), (b) global mean surface temperature (K), (c) ELOTC (K), (d) MMCI (m s^{-1}), and (e) PRWI (kg m^{-2}), computed over the same periods. All indices are defined in section 2. The black cross in each scatterplot marks the MMM. As explained in the text, all the 34 available CMIP6 models are used here, with 1 to 50 simulations (see Table S1). For each panel, the correlation and the corresponding p value are computed as described in section 2. The red outline of the panel means that the correlation is significant at the 95% confidence level ($p < 0.05$). Temperature and precipitation change are computed as the difference of climatological means between the end of the historical period (1979–2014) and the early industrial period (1850–75).

significant, relationship with the WYI change (Fig. 2a). However, the origin of the dispersion of the dynamic component of the ISMR remains unexplained. Indeed, in the future projections, ISMR and WYI changes are both significantly correlated with ELOTC (Jin et al. 2020), indicating a role for land–sea thermal contrast. This is not the case over the historical period (Fig. 2c for IMSR and not shown for WYI). This suggests that the mechanisms in the historical period and in projections differ. This difference may be due to the fact that aerosol forcing is strong over the historical period and does not allow for the emergence of a strong land–sea contrast.

We have shown that the intermodel spread of ISMR change is mainly related to the intermodel spread of the dynamic component. However, we lack explanations as to the origin of the intermodel spread of this dynamic component. A first approach is to look at the local scale. Hence, in the next subsection we investigate the role of the model's mean biases and variability over India to explain ISMR changes.

c. *Local relationships between ISMR bias and change over the historical period*

Figure 3 explores the linear dependence between ISMR change with local precipitation and temperature biases over India. Figures 3a and 3d show that in spite of the strong intermodel spread of ISMR biases in mean and temporal variability (e.g., standard deviation), there is no significant relationship between these biases and the ISMR change at the 95% confidence level. Hence, selecting models based on their performance in reproducing the present-day precipitation climatology and variability (Katzenberger et al. 2021) is not a discriminating criterion for how they simulate ISMR change. As for precipitation, there is also no significant relationship ($p > 0.05$) between climatological and variability biases of Indian surface temperature and ISMR change (Figs. 3b,e). On the other hand, Fig. 3c highlights a significant and expected relationship between climatological biases of surface temperature and precipitation over India. This can be explained by a reduced cooling effect (e.g., less clouds and evaporation) due to a deficit of local precipitation over India. Note, nevertheless, that an anomalous land warming could enhance the regional land–sea contrast, thereby inducing an opposite precipitation bias (Jin and Wang 2017), but this effect does not seem to dominate here, consistent with the weak correlation between ISMR and ELOTC changes (Fig. 2c).

To conclude, no obvious link was found at the local scale between the spread of local rainfall/temperature biases and ISMR change. This lack of linkage could be due to the fact that the changes in precipitation and biases are averaged over India where there are potentially inhomogeneities and error compensations for both biases and changes. It could also be that there are simply no relationships at the local scale. To discriminate between these two hypotheses, we need to zoom out from the local scale.

d. *Global changes of surface temperature and precipitation over the historical period*

Figure 4a displays the JJAS precipitation historical changes over the whole globe. Central America, Sahel, and East Asia, which are three major monsoon regions, all exhibit a strong

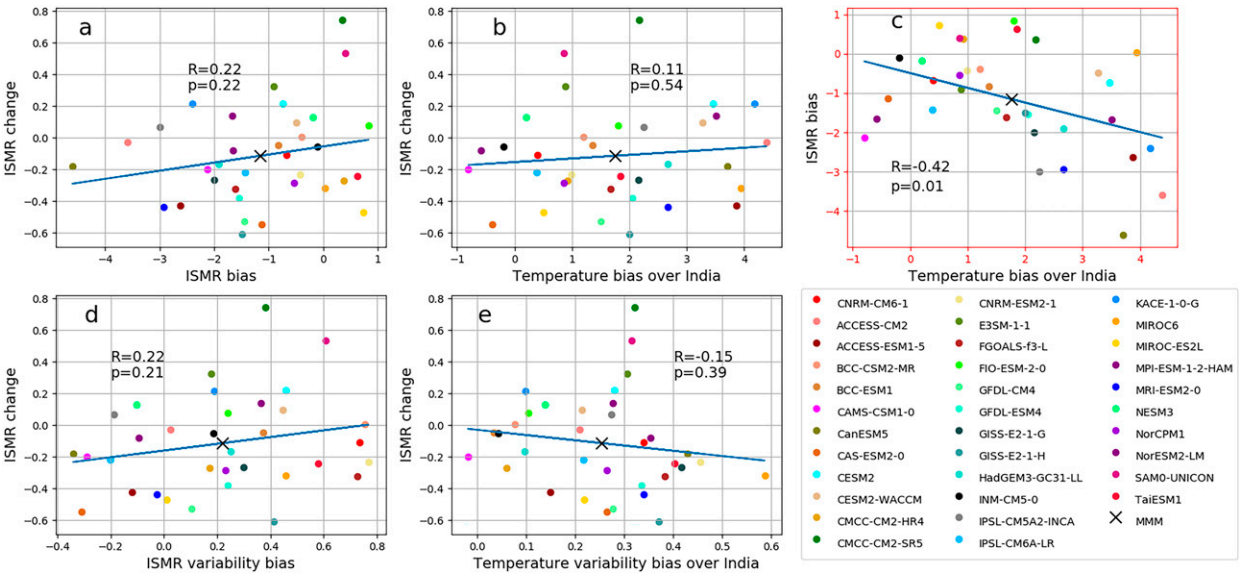

FIG. 3. Scatterplots of ISMR change (mm day^{-1}), respectively, with (a) mean ISMR bias (mm day^{-1}), (b) mean temperature bias over India (K), (d) ISMR standard deviation bias (mm day^{-1}), and (e) temperature standard deviation bias over India (K). Temperature biases are calculated over India, which corresponds to the same domain as the one used for ISMR. Temporal standard deviation in (d) and (e) is computed for each individual historical member and averaged for each model in case of several members. (c) Scatterplot of mean ISMR bias and mean surface temperature bias over India to illustrate local interaction between temperature and precipitation bias over India. The correlation and its associated p value for each pair of model series are indicated in each panel. The red outline means that the correlation is significant at the 95% confidence level ($p < 0.05$). Crosses indicate the MMM position in each scatterplot.

drying over the historical period. Figure 4a also displays a strong drying over the north subtropical Atlantic and over the Maritime Continent, both accompanied with a strong spread across models (Fig. 4b). The Pacific Ocean presents notable wetting over the South Pacific convergence zone (SPCZ) and over the western part of the ITCZ, which is located at 10°N over this region during the boreal summer and some drying in between. Furthermore, the intermodel spread of precipitation change in the Pacific Ocean is particularly strong over the warm pool and the convergence zones (SPCZ and ITCZ) forming a double ITCZ structure (Fig. 4b). Figures 4a and 4b also display a large intermodel spread of precipitation change over India, while the MMM change is not very strong and quite inhomogeneous. These features indicate a strong disagreement between models, but also indicate that averaging precipitation change over India may not be representative of ISMR change. This justifies the need to take into account the spatial pattern of rainfall changes over India when looking for relationships between biases and ISMR change.

Looking at the warming signal (Fig. 4c), an interesting feature is that the SST gradient along the equatorial Pacific (see its definition in Table 1) is enhanced toward the end of the historical period in 25 of 34 models (not related to the models with more than one member) and in the MMM (0.1 K). This latter result is at odds with the CMIP5 MMM, but it is in line with observed trends (Lian et al. 2018). Hence, CMIP6 models show a better agreement with observations than the previous generation, but they still underestimate the enhancement of the equatorial Pacific SST gradient (0.3 K). This pattern is complex and not "La Niña–like" or "El Niño–like" as discussed in Lian et al. 2018. It is rather "El Niño Modoki–like" (Ashok et al. 2007) with a stronger warming over the central Pacific, an intermediate warming over the warm pool, and a weaker warming signal over the eastern equatorial Pacific. Furthermore, the Pacific warming pattern, and hence the change in the SST gradient, is quite different between annual and JJAS mean averages (supplemental Fig. S4), highlighting that focusing on yearly ENSO patterns only may be misleading for understanding ISMR changes. It is necessary to look at the seasonal scale of change in the Pacific to fully understand the interactions with ISMR.

There is a strong intermodel spread of surface temperature change over the whole Eurasian continent and specifically over the Tibetan Plateau, which have both been suggested as important driving factors for ISMR projections (Fig. 4d; Ge et al. 2017; Wang et al. 2020). The largest spread of land temperature changes among models occurs over central Africa, North America, and north of India. Over the ocean, intermodel spread is high at mid- to high latitudes of both hemispheres and also in the eastern equatorial Pacific.

We now have an overview of the MMM spatial changes in surface temperature and precipitation over the historical period, as well as an idea of the areas with the highest disagreement between the models. In the following subsection, we will focus on the biases of these two variables and highlight the regions where the intermodel spread is important in CMIP6

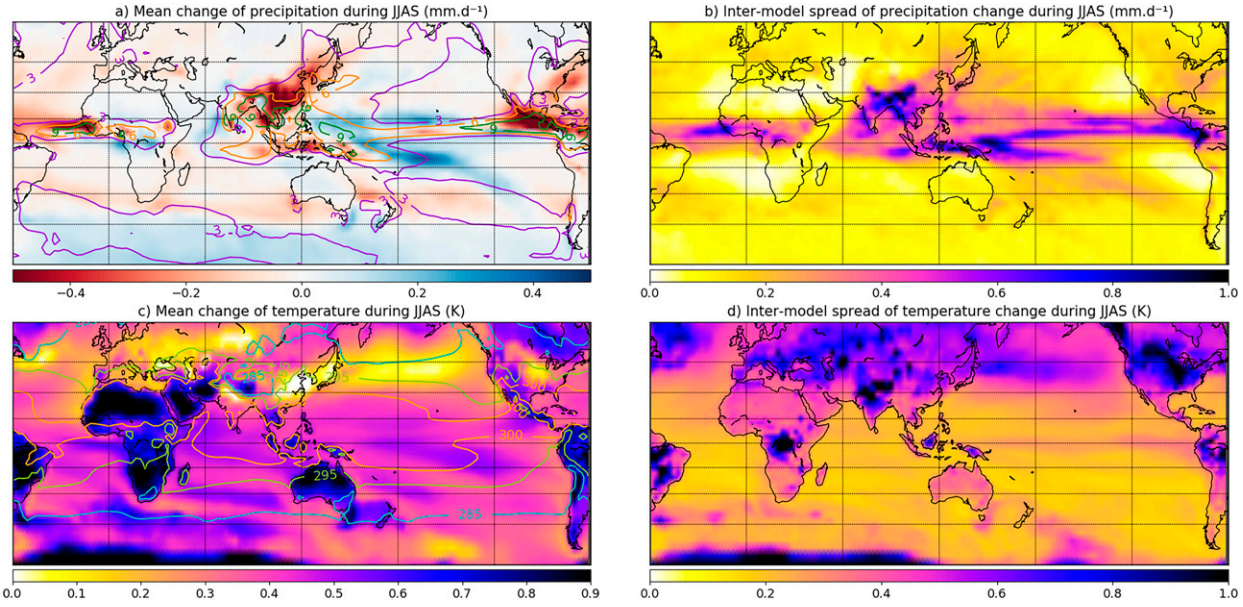

FIG. 4. JJAS MMM and intermodel spread of (top) precipitation (mm day^{-1}) and (bottom) surface temperature (K) changes computed for the 34 CMIP6 models. (a) MMM precipitation change. (b) Intermodel spread of precipitation. (c) MMM surface temperature change. (d) As in (b), but for surface temperature. Contours in (a) are for JJAS mean precipitation from GPCP (contour interval is 3 mm day^{-1}) and in (c) are for JJAS mean surface temperature from ERA-Interim (285 K, blue; 295 K, green; 300 K, orange contours). Temperature and precipitation changes are computed as the difference of climatological means between the end of the historical period (1979–2014) and the early industrial period (1850–75). See section 2 for details.

models, as we seek to establish a link with the spread in the ISMR change.

e. *An overview of climatological rainfall and temperature biases in CMIP6 models*

Figures 5a and 5b first show that India suffers on average from an important dry bias with a large intermodel spread. This dry bias is very pronounced over northern India, while it is almost absent in the south. This is consistent with the tendency of models to produce an ITCZ located 10° south of the observed location in most monsoon regions (Choudhury et al. 2022). In the Indian sector, this southward shift of the ITCZ may be due to warm SST biases over the southwest IO or along the equator (Bollasina and Ming 2013; Prodhomme et al. 2014; Annamalai et al. 2017) and/or to cold surface temperature biases over adjacent deserts (Fig. 5c; Terray et al. 2018; Sooraj et al. 2019). Both the arid regions to the west of India and the western IO have large mean biases and present a strong intermodel spread of surface temperature (Fig. 5d); they are therefore potential candidates for modulating ISMR changes.

Focusing now on remote regions, the Pacific Ocean displays an erroneous double ITCZ structure in both MMM (Fig. 5a) and intermodel spread (Fig. 5b) of precipitation bias. These errors have been typical and prominent biases of CGCMs from CMIP3 to CMIP6 even if they have been shown to be slightly reduced in CMIP6 (Tian and Dong 2020). Interestingly, both the mean and intermodel spread patterns of rainfall changes in Figs. 4a and 4b are also reminiscent of this double ITCZ bias. The equatorial Pacific is also characterized by a cold tongue bias extending from the warm pool to the eastern Pacific, and the Maritime Continent is marked by a warm bias. The upwelling regions off the Chilean and Peruvian coasts show an important warm bias that spreads northward and meets the cold tongue bias at the equator. The equatorial Atlantic also presents an important wet bias. It is attributed to the strong warm bias over the southeastern Atlantic (Fig. 5c), which causes a southeastward shift of the ITCZ over the Atlantic (Richter and Tokinaga 2020). However, as the warm Atlantic bias does not present an important intermodel spread, it is unlikely to explain the equatorial spread of precipitation alone at least in a simple linear framework. Again, continental biases, especially those over the Sahara, or erroneous combined land–ocean temperature gradients are more plausible candidates (Terray et al. 2018; Sooraj et al. 2019). Using CMIP5 models, Shamal and Sanjay (2021) have suggested that these intermodel spreads of temperature and rainfall biases in the Atlantic sector may provide a strong observational constraint for reducing the uncertainties of ISMR projections. We will test this hypothesis with CMIP6 and the historical period in the next section. Finally, Fig. 5d displays a very strong intermodel spread along with a cold bias in the MMM over the Himalayas, which may arise from the variety of the model's resolution and orography as it is a limiting factor in this region of complex orography (Lalande et al. 2021).

To conclude, given the large intermodel spread of surface temperature and rainfall biases, including both land and ocean, and the complexity in existing teleconnections to ISMR (Chowdary et al. 2021), we will next track the origins of the spread of ISMR change within the whole tropics. To this end,

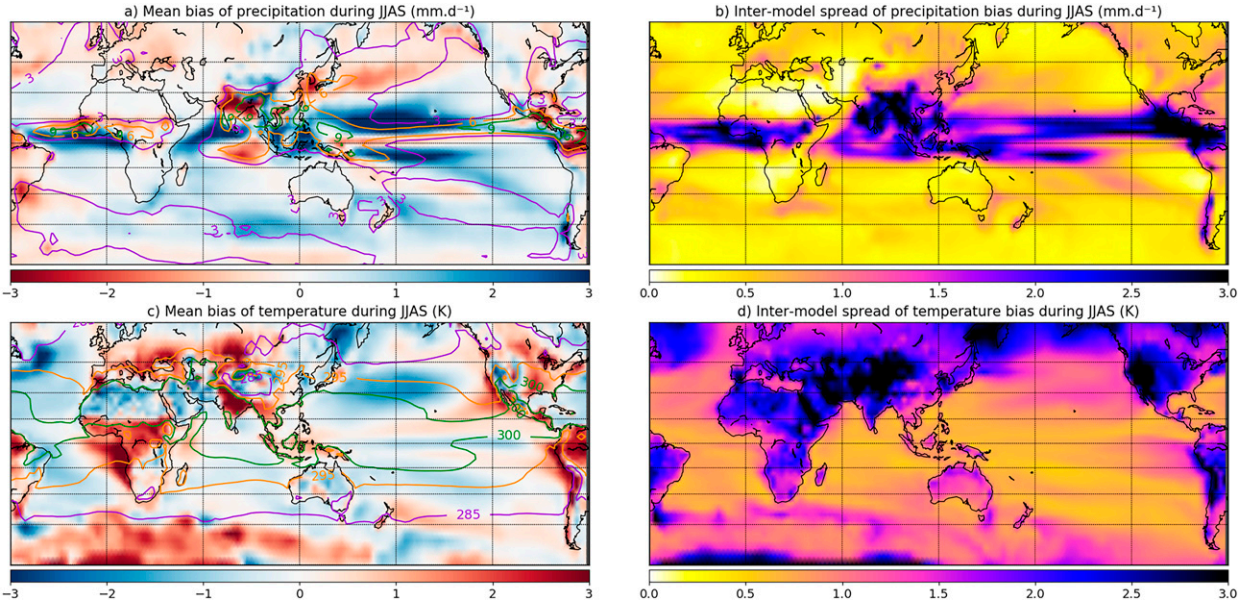

FIG. 5. Boreal summer MMM and intermodel spread of (top) precipitation (mm day^{-1}) and (bottom) temperature (K) biases computed over the 1979–2014 period for 34 CMIP6 models. (a) MMM precipitation bias with respect to GPCP. (b) Intermodel spread of precipitation. (c) MMM temperature bias with respect to ERA-Interim. (d) As in (b), but for temperature. Contours in (a) are for JJAS mean precipitation from GPCP (contour interval is 3 mm day^{-1}) and in (c) are for JJAS mean temperature from ERA-Interim (285 K, purple; 295 K, orange; 300 K, green contours).

we will investigate the dominant modes of covariance between tropical temperature or precipitation biases and ISMR changes with the help of MCAs. This method allows us to move away from spatial averaging over India and to explore the possible link between the pattern of precipitation change over India and tropical biases elsewhere.

4. Remote impact of biases on ISMR historical changes

a. *Spatial patterns of biases and rainfall changes from maximum covariance analysis*

We computed two MCAs, one between rainfall changes over India (7°–20°N and 65°–95°E; land only) and surface temperature biases within the tropical band (30°S–30°N) (Figs. 6a,b), and the other between rainfall change over India (same region) and tropical precipitation biases (Figs. 6c,d). A brief introduction to MCA is provided in Text S1 of the supplemental material for convenience, and more details can be found in Bretherton et al. (1992). We only study the leading coupled mode for each of these MCAs, as they describe a major part of the covariability between the original fields (Table 2), and they are well separated from the remaining MCA modes (not shown).

The heterogeneous maps of rainfall changes over India are spatially homogeneous and very similar in both computations (Figs. 6a,c). Consistently, the correlation between the singular variable (SV) series (e.g., expansion coefficient series) associated with the rainfall change patterns over India in both MCAs is 0.99. The SV series of precipitation changes over India in each MCA are also strongly correlated with the average index ISMR ($r = 0.95$ and 0.94; see Table 2). This latter result confirms that tropical precipitation and surface temperature biases (Figs. 6b,d) are covarying with the Indian monsoon as a whole despite the fact that MMM rainfall changes are inhomogeneous over India (Fig. 4a). The rainfall change patterns from the MCAs (Figs. 6a,c) are also very close to the first EOF mode of ISM rainfall change (not shown). The spatial structures of the leading modes from EOF and MCA are correlated with $r = 0.99$, and the explained variances by these modes are again very close (42% for the first mode of EOF and 39% for both MCAs). These features suggest that the patterns of bias identified in Figs. 6a and 6c are linked with the main mode of intermodel spread of ISM rainfall change, which further motivates a detailed analysis of these modes.

The first modes of the MCAs between surface temperature and precipitation biases with ISM rainfall changes have a square covariance fraction (SCF) of 47% and 40%, respectively, and they have similar normalized root-mean-square covariance (NC) statistics (see Text S1 in the supplemental material for a more detailed definition of this MCA statistic), suggesting that the precipitation and surface temperature biases have a statistical relationship with Indian rainfall change of similar strength (Table 2). Moreover, the correlations between the SV series corresponding to the leading patterns of precipitation and temperature biases and those of rainfall changes in each MCA are quite similar too (0.75 and 0.67; see Table 2), which corroborates that a similar strong relationship exists between biases and ISMR changes. Note that the correlation between the SV series associated with the leading bias pattern in each MCA is $r = 0.67$ ($p < 0.01$). This further shows that a linear relationship may also exist between the leading patterns of rainfall and temperature biases

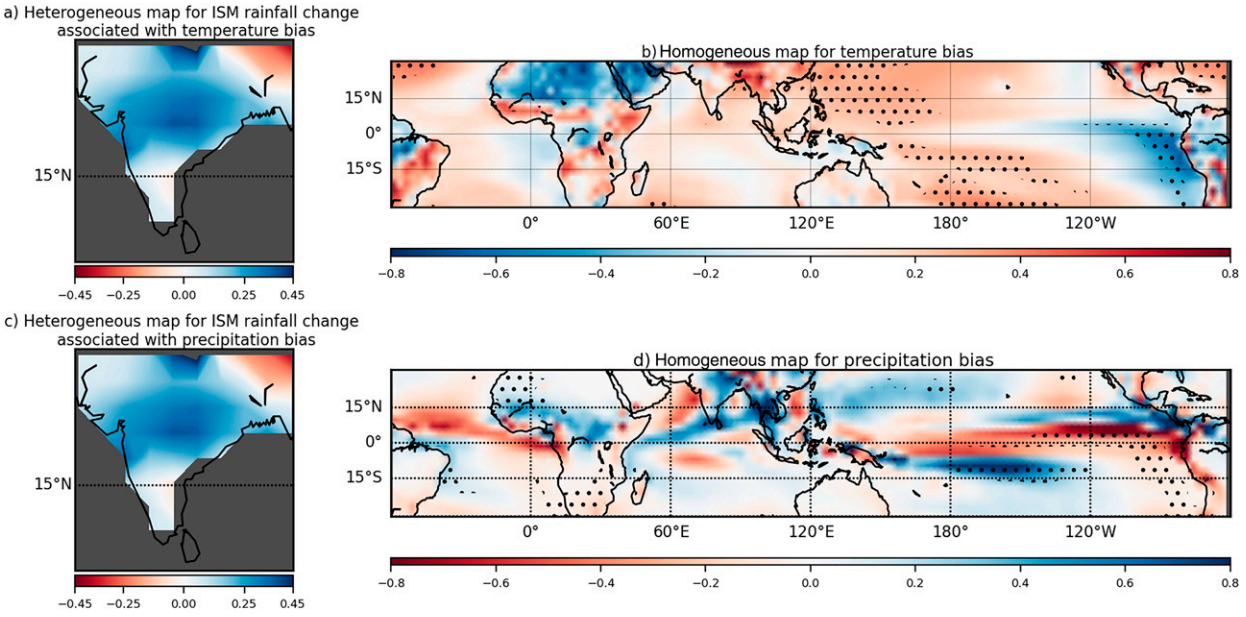

FIG. 6. (a) Heterogeneous and (b) homogeneous maps obtained from the MCA performed between the surface temperature bias of the 34 climate models and the ISM precipitation changes detected over the historical period in the same 34 models. (c),(d) As in (a) and (b), but for the MCA computed between the precipitation bias and the ISM precipitation change. Dotted points indicate significant correlations at the 95% confidence level between the respective SV and gridpoint time series. See Text S1 in the supplemental material for a short introduction to MCA or Bretherton et al. (1992) for more details on SVs (e.g., expansion coefficient series), heterogeneous and homogeneous maps, and the various statistics produced by MCA.

associated with ISM rainfall changes. In other words, this suggests the existence of coupled ocean–atmosphere and/or land–atmosphere biases, which may modulate ISMR changes over the historical period.

Associated with an increase of precipitation over India from the beginning to the end of the historical period (Fig. 6a), Fig. 6b exhibits a strong cooling over the Sahara and Arabian Deserts extending to the west of India, while the rest of India presents a strong warm bias. This spatial inhomogeneity of the intermodel temperature bias over India could explain the lack of relationship between the intermodel spread of ISMR change and Indian surface temperature bias shown in Fig. 3b. The warm bias extends to eastern and southeastern Asia, which, as mentioned earlier, experience a significant drying trend. From an oceanic perspective, Fig. 6b presents a well-defined equatorial SST gradient in the Pacific, with a cooling in the east and a warming in the west, but mainly off the equator and up to the subtropics. This pattern of SST bias in the Pacific is reminiscent of a La Niña–like SST mean pattern. Interestingly, from a statistical perspective, this La Niña–like SST pattern is significant (e.g., see the dotted areas in the Pacific) in contrast to the temperature gradient over land described above. This is physically consistent with the increase of precipitation over India in Fig. 6a as seen for the interannual time scale framework (Chowdary et al. 2021).

From the atmospheric perspective, the leading pattern of model precipitation biases presents strong signals over the

TABLE 2. Statistics of the MCAs between surface temperature or precipitation biases with Indian rainfall change shown in Fig. 6. All correlations in the last four columns are significant at the 99% confidence level. See text and Text S1 in the supplemental material for more details on the SCF and NC statistics.

	Explained variance of Indian rainfall change	SCF	NC	Correlation between SVs of rainfall change over India and ISMR change	Correlation between SV of bias and SV of rainfall change over India	Correlation between SVs of surface temperature and precipitation bias from the two MCAs	Correlation between SVs of rainfall change over India from the two MCAs
Pr bias; Indian rainfall change	39.4%	40%	12.5%	0.95	0.75	0.67	0.99
Ts bias; Indian rainfall change	39.5%	47%	12.9%	0.94	0.67		

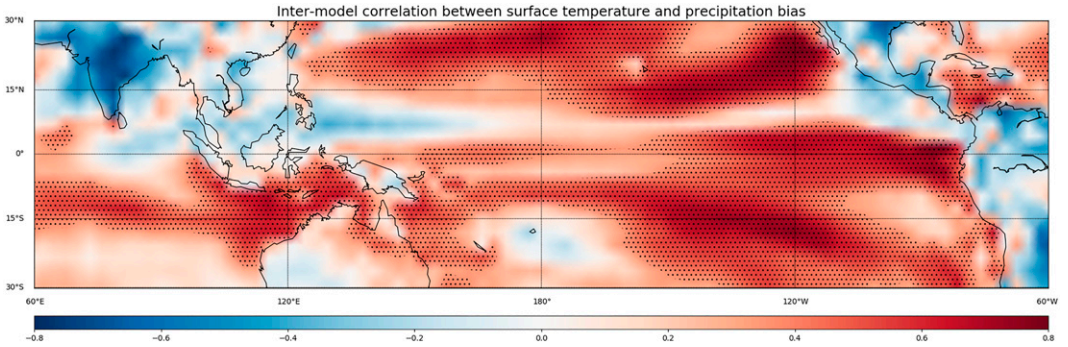

FIG. 7. Intermodel correlation between surface temperature and precipitation biases computed at every grid point in the Indo-Pacific region for the 34 CMIP6 models (see supplemental Table S2 for the list of models). Dotted points indicate grid points where the correlation is significant at the 95% confidence level.

whole tropics. First, Fig. 6d shows a double ITCZ structure over the Pacific Ocean consistent with the intermodel spread of precipitation biases discussed in section 3e. Statistical significance is moreover well defined along the equatorial Pacific and the SPCZ (Fig. 4d). Models showing a positive ISM rainfall change typically also present a strong dry bias (more precisely a reduced wet bias; see Fig. 5a) over the equatorial Atlantic, accompanied by a wet bias (e.g., a reduced dry bias) over the Sahel and central Africa, which corresponds to a northward shift of the ITCZ. This signal therefore strongly modulates the MMM rainfall bias shown in Fig. 5a over the Atlantic region. The bias pattern is complex over the IO, with a tripolar structure composed of an enhanced wet bias between 0° and 10°N, surrounded by a dry bias north and south of this band. Note that over the Indian and Atlantic regions, not many areas exhibit statistically significant gridpoint correlation in contrast to what is detected over the tropical Pacific.

To further illustrate the leading role of the tropical Pacific biases in generating intermodel spread in ISMR changes over the historical period, we computed MCAs with surface temperature and precipitation biases restricted to the tropical Pacific (see supplemental Fig. S5). The results are very similar to the Pacific structure described in Figs. 6b,d, but with higher correlations ($r > 0.85$) between the SV model series associated with the patterns of biases in each MCA. This points out the importance of Pacific biases described above and also again to the key role of ocean–atmosphere coupling in this basin for ISM rainfall changes as simulated by CMIP6 models.

As mentioned above, there is a strong relationship between the pattern of surface temperature and precipitation biases in the Indo-Pacific domain. Figure 7 explores this relationship by correlating precipitation and surface temperature biases at every grid point. The negative correlations over land are expected and consistent with the analysis of section 3c. They arise from a reduced cooling effect associated with a deficit of local precipitation and indicate that the atmosphere drives the coupling between surface temperature and precipitation biases. Over the ocean, the sign and the intensity of the correlation between these two variables are spatially variable due to the complexity of local ocean/atmosphere processes in each basin. Correlations are highest over the equatorial and subtropical areas in the Pacific. The Pacific Ocean mostly displays a positive correlation except along the Mexican coast, the Philippine Sea, and off the coast of Australia. The correlation is particularly strong in the same regions, which exhibit gridpoint statistical significance in Figs. 6b and 6d. This is especially true over the eastern Pacific, indicating that enhanced oceanic warm bias is associated with a wet bias over this region and vice versa across the models. This suggests that surface temperature biases drive the atmosphere biases over this region.

Therefore, since the biases in the tropical Pacific Ocean, particularly along the equator, are correlated with the ISM rainfall changes (Figs. 6b,d), and there is a tight coupling between the ocean and atmosphere biases over the Pacific (Fig. 7), we will focus in the following subsection on the impact of the bias affecting the equatorial Pacific SST gradient as a possible key factor for explaining the intermodel spread of historical change of this SST gradient over the equatorial Pacific and, in turn, ISMR changes.

b. *Relationship between intermodel spread of ISMR change and the equatorial SST gradient in the Pacific*

To explore the role of equatorial Pacific SST gradient biases, we first define an index of the zonal SST gradient as the SST difference between the western and eastern equatorial Pacific (see Table 1). A positive value of this zonal SST gradient index indicates a La Niña–like situation in both the SST bias and change spatial patterns over the tropical Pacific. There is a significant correlation between the SST gradient bias index and ISMR change ($r = -0.47$; $p < 0.01$), which confirms our previous interpretations on the role of tropical Pacific biases, especially along the equator, from the MCAs, and this subsection will look at the underlying mechanisms behind this statistical relationship.

First, Fig. 8a shows that models that present a La Niña–like bias have a tendency to produce a strong cooling over the equatorial eastern Pacific and a warming over the equatorial western Pacific by the end of the historical period. The correlation between the equatorial Pacific SST gradient (as defined in Table 1) bias and change confirms the existence of this strong and significant linear relationship between bias and

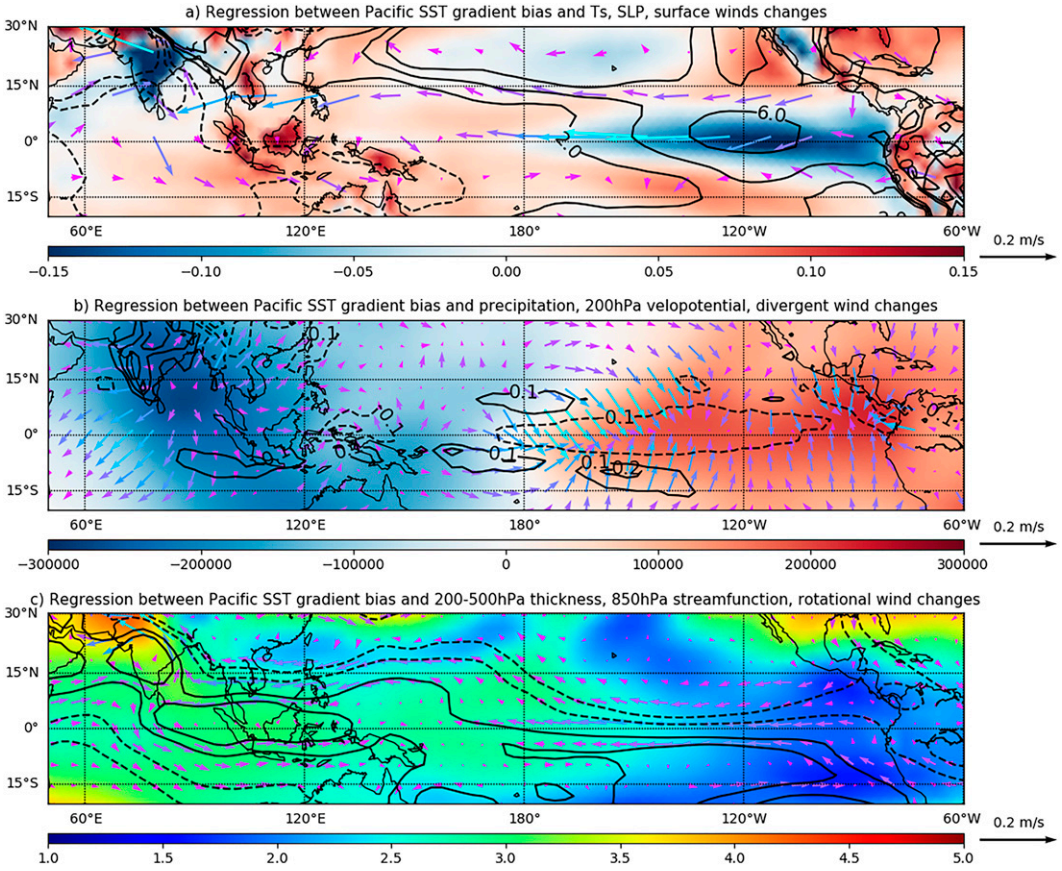

FIG. 8. Intermodel regressions against the equatorial Pacific SST gradient bias of (a) changes in SST (color shaded; K K^{-1}), sea level pressure (contour interval: 2 hPa K^{-1}) and wind at 850 hPa (vectors; m s^{-1} K^{-1}); (b) historical changes of velocity potential at 200 hPa (color shaded; m^2 s^{-1} K^{-1}), precipitation (contour interval: 0.1 mm day^{-1} K^{-1}), and divergent wind at 200 hPa (vectors; m s^{-1} K^{-1}); and (c) historical changes in 200–500-hPa thickness (color shaded; m K^{-1}), 850-hPa streamfunction (contour interval: 30 000 m^2 s^{-1} K^{-1}), and rotational wind at 850 hPa (vectors; m s^{-1} K^{-1}). The colors of the arrows in all three panels vary from purple to cyan according to the intensity of the wind speed for readability. In (a), only one vector of two is shown also for readability.

historical changes ($r = 0.66$; $p < 0.01$). In other words, models that simulate a La Niña–like SST gradient (positive gradient bias) tend to produce La Niña–like SST change over the Pacific Ocean and vice versa. According to Fig. 8, the SST gradient bias correlates more strongly with SST changes in the eastern equatorial Pacific. Furthermore, the bias of the Pacific SST gradient is more correlated with the SST bias in the eastern Pacific than in the western (supplemental Fig. S6). This suggests that, over the historical period and for CMIP6 models, the eastern equatorial Pacific plays a dominant role in shaping the change of the equatorial SST gradient as compared to the west. This is reminiscent of the ocean dynamical thermostat (ODT) mechanism (Clement et al. 1996).

Consistently, models with a La Niña–like SST gradient bias also show an increase in the SLP gradient across the Pacific via an increase in pressure in the east and a decrease in the west during the historical period (Fig. 8a). These changes in SLP and SST gradients are accompanied with an increase in easterly winds over the tropical Pacific, with all three variables being related to each other through the Bjerknes feedback (Bjerknes 1969).

These changes in surface variables are accompanied by changes at higher levels in the atmosphere (Fig. 8b) as the surface communicates with higher atmospheric levels via the latent heat release and the Walker circulation. An anomalous positive equatorial SST gradient in the Pacific induces an intensification of the Walker circulation, as well as a westward shift of its ascending branch (see supplemental Fig. S7). Indeed, Fig. 8b shows an increase in upper-level wind divergence over the Bay of Bengal and India, which implies more intense convective activity and release of latent heat. On the other hand, over the eastern Pacific we observe an increase in upper-level wind convergence, which is accompanied by an increase in subsidence and therefore a reduction in precipitation by enhanced atmospheric stability.

The intermodel spread of precipitation changes over the eastern and central Pacific, associated with the intermodel spread of the equatorial Pacific SST gradient, induces an intermodel spread of latent heat release aloft which propagates

eastward in the form of a Kelvin wave over the Atlantic (not shown in Fig. 8c) and westward across the subtropical Pacific in the form of Rossby waves. The latter can be seen in Fig. 8c with the equatorially symmetric response of the tropospheric thickness change. Models that tend to show a positive bias in the SST equatorial gradient (e.g., La Niña–like anomalous pattern) are associated with an anticyclonic circulation around 15°N in the western Pacific at the end of the historical period (Fig. 8a), which promotes the moisture transport across the Bay of Bengal to India through enhanced southerlies at the surface (Figs. 8a,c). This increase of the meridional circulation can also be evidenced by the increase of the zonal tropospheric thickness gradient around India, which strengthens the vertical shear of the meridional wind according to the thermal wind relationship (Dai et al. 2013). Note that these relationships work conversely for models showing a negative bias of the SST equatorial gradient in the Pacific, as our analysis is linear. This mechanism is further supported by the correlation between the change in precipitation over the central Pacific (5°S–5°N; 180°–100°W) and the change in the MMCI ($r = -0.45$; $p < 0.01$), which was itself significantly linked to the intermodel spread of ISMR change in section 3b.

In summary, a mean bias in the equatorial Pacific SST gradient seems to modulate the ISMR change ($r = -0.47$; $p < 0.01$) by physical mechanisms very similar to those operating in the ENSO–monsoon teleconnection (Roy et al. 2019). Indeed, the intermodel spread of the equatorial Pacific SST gradient bias in the CMIP6 models modulates the historical change in this gradient, which is accompanied by cascading effects through the Bjerknes feedback, leading to a change in the Walker circulation that favors convection over India when the initial bias is more La Niña–like and vice versa. In other words, models that simulate a La Niña (El Niño)–like SST gradient tend to produce La Niña (El Niño)–like changes over the Pacific Ocean.

5. Conclusions

The impact of tropical temperature and precipitation biases on simulated changes of ISMR has been analyzed here using historical simulations of 34 coupled models from CMIP6 in order to unravel the potential roles of these biases in the large uncertainties and intermodel spread affecting ISMR simulations and projections.

a. Summary

Our results first confirm that the skill of CGCMs at reproducing ISMR climatology and trend has increased from CMIP3 to CMIP6, but the latest models still exhibit significant biases during JJAS (Jin et al. 2020; Wang et al. 2020). In particular, ISMR still suffers from a persistent mean dry bias. In terms of historical changes, the MMM from CMIP6 models still struggles to reproduce the observed post-1950 drying trend of ISMR, but the agreement of CMIP6 MMM with observations is better over the recent decades (1990–2014) during which both AIR and IMD datasets present a significant wetting trend (Jin and Wang 2017; Roxy 2017). However, both observed datasets and individual CMIP6 models disagree on the amplitude of this wetting trend. Over this wetting period, the models present a very large intermodel spread, and 40% of them produce a (nonobserved) drying trend. Our analysis demonstrates that this cannot simply be attributed to internal variability as the intermodel spread is also prominent in multimember averages in which internal variability plays a secondary role.

On a broader scale, CMIP6 models also present similar errors as previous generations: the Pacific Ocean displays an erroneous double ITCZ (Tian and Dong 2020), an equatorial Pacific cold tongue bias (Li et al. 2016), and warmer-than-observed SST in eastern boundary upwelling systems, especially in the southeast Pacific and Atlantic Oceans (Farneti et al. 2022). On an annual basis, but even more so in boreal summer, the Pacific Ocean shows an El Niño Modoki pattern of change in the historical period. However, the east–west equatorial SST gradient is increased in the MMM, suggesting also a La Niña–like pattern of change. These results are not in line with those of CMIP5, where many models agreed on an El Niño–like warming over the historical period, nor are they consistent with observations (Lian et al. 2018).

Following this assessment of the performance of the models in CMIP6, we answered the three questions that had been raised in the introduction concerning the intermodel spread of historical change ISMR:

1) Is there a local link between climatological biases over India and ISMR change? We demonstrated that temperature and rainfall climatology (and variability) biases over India cannot be used to constrain the intermodel spread of ISMR changes despite that these local biases also present a large intermodel spread. This is consistent with past investigations on CMIP5 (Racherla et al. 2012).
2) Are there links with some remote biases over land or the tropical oceanic basins? The MCAs suggest that tropical rainfall and temperature biases play a leading role in the intermodel spread of ISMR rainfall changes over the historical period, producing a similar and uniform rainfall change over India. The MCA results also confirm that the local biases are not key to reducing the uncertainties in ISMR changes. Further analysis demonstrates that remote coupled ocean–atmosphere biases in the Pacific Ocean play a dominant role. Furthermore, the strong positive correlation between local temperature and precipitation biases in the Pacific suggests that the ocean is driving the coupled biases. Consequently, we focused on the role of the bias of the equatorial SST gradient and found that the climatological background state for each model plays a pivotal role in determining the Pacific mean state change over the historical period with the eastern equatorial Pacific playing a leading role in these interactions (Fig. 6b).
3) By which physical processes do local and/or remote biases influence ISMR historical evolution? Our analysis suggests that models having a La Niña–like SST gradient bias tend to favor a La Niña–like change and, conversely, an El Niño–like bias promotes an El Niño–like change. Therefore, by modulating the change of the SST gradient

in the Pacific, the bias of this gradient impacts the local rainfall and the Walker circulation changes, which result in ISM rainfall changes through teleconnection mechanisms very similar to those associated with the ENSO–ISM teleconnection (Roy et al. 2019; Chowdary et al. 2021). The equatorial Pacific SST gradient bias also modulates changes of latent heat release (associated with the local rainfall changes) that propagate westward in the form of Rossby waves into the subtropical North Pacific Ocean. For La Niña–like models, this creates low-level anticyclonic anomalies 10° north of the Maritime Continent and changes the midtropospheric temperature gradient westward of the rainfall change in the central Pacific. Conversely, for El Niño–like models in which the Pacific equatorial SST gradient is reduced, the changes of this midtropospheric temperature gradient are reversed during the historical period. This finally leads to a modulation of the meridional monsoon circulation across the CMIP6 models, which also results in an intermodel spread of ISM rainfall and MMCI changes. The modulation of the meridional monsoon circulation by biases in the Pacific Ocean has already been suggested to play a key role in the intermodel spread of ISMR projections in CMIP5 (Li et al. 2017). However, and although the circulation patterns involved here are similar, the underlying mechanisms we suggest for the historical period are different; they involve mainly the eastern equatorial Pacific, while the role of the western Pacific is dominant in the future as diagnosed by Li et al. (2017).

b. *Discussion and perspectives*

As summarized in Lian et al. (2018), the changes of the equatorial Pacific SST gradient can be understood in an atmospheric or oceanic framework. On the one hand, the atmospheric framework links a reduction of the equatorial Pacific gradient to the weakening of the tropical and Walker circulations under a GHG forcing scenario (Held and Soden 2006). On the other hand, the oceanic framework leads to an increase of the gradient under global warming (Clement et al. 1996). The oceanic framework is based on the ODT mechanism, which refers to the damping effect of the oceanic upwelling in the eastern equatorial Pacific for a given forcing through heat divergence (Clement et al. 1996). Here, we suggest that a positive SST gradient bias is associated with an overly pronounced upwelling in the eastern Pacific, which causes an overestimation of the ODT mechanism, leading to a reinforcement of the Pacific equatorial SST gradient over the historical period and vice versa for models with a negative SST gradient bias in the equatorial Pacific. Note that a poor sampling of "observed" internal variability can also play an important additional role in the mismatch between observations and simulations. Recent results show that a correct representation of the internal variability requires large ensemble simulations, and when this is done the observed Pacific trend lies in the spread of the simulated internal variability (Watanabe et al. 2021).

Future studies should investigate in more detail how the equatorial biases in the Pacific can lead to a misrepresentation of the forced response (Lian et al. 2018) and whether these biases can be understood solely by intrinsic modeled errors of the Pacific coupled system or if these biases can be induced by remote errors, for example, those in the Atlantic or Indian basins (McGregor et al. 2018; Shamal and Sanjay 2021; Terray et al. 2021, 2023).

In a future study, the relationship between the Pacific equatorial SST gradient bias and ISMR change could be further tested using SST nudging experiments to corroborate the mechanisms that we proposed. We could also investigate whether the relationships we found over the historical period between the Pacific equatorial SST gradient biases and ISMR would still hold in CMIP projections. Indeed, we have suggested that the ODT mechanism links the equatorial Pacific gradient bias and change, but this relationship may diminish on longer time scales because the ODT mechanism is described as a rapid response of the Pacific Ocean to radiative forcing (Heede et al. 2020), as the ODT mechanism is weakening with the progressive warming of the equatorial thermocline (Luo et al. 2017).

Acknowledgments. Pascal Terray and Juliette Mignot are funded by Institut de Recherche pour le Développement (IRD; France). Analysis was done with Python (https://www.python.org/) and the STATPACK and NCSTAT softwares (https://terray.locean-ipsl.upmc.fr/software.html). This work benefited from ESPRI (https://mesocentre.ipsl.fr), which is supported by CNRS, Sorbonne University, Ecole Polytechnique, and CNES and through national and international grants. We also acknowledge funding from the ARCHANGE project of the "Make Our Planet Great Again" program (ANR-18-MPGA-0001; France) and from JPI Climate/JPI Oceans ROADMAP project (ANR-19-JPOC-003).

Data availability statement. The study is based on the outputs of CMIP6. These are publicly available upon registration on the data portal of the Earth System Grid Foundation (ESGF; https://esgf-node.ipsl.upmc.fr/search/cmip6-ipsl/). ERA-Interim is publicly accessible upon registration on the ECMWF data portal (http://apps.ecmwf.int/). The GPCP data are publicly accessible (https://psl.noaa.gov/data/gridded/data.gpcp.html).

REFERENCES

Adler, R. F., and Coauthors, 2003: The Version-2 Global Precipitation Climatology Project (GPCP) monthly precipitation analysis (1979–present). *J. Hydrometeor.*, **4**, 1147–1167, https://doi.org/10.1175/1525-7541(2003)004<1147:TVGPCP>2.0.CO;2.

Allan, R. P., and Coauthors, 2020: Advances in understanding large-scale responses of the water cycle to climate change. *Ann. N. Y. Acad. Sci.*, **1472**, 49–75, https://doi.org/10.1111/nyas.14337.

Annamalai, H., B. Taguchi, J. P. McCreary, M. Nagura, and T. Miyama, 2017: Systematic errors in South Asian monsoon simulation: Importance of equatorial Indian Ocean processes.

J. Climate, **30**, 8159–8178, https://doi.org/10.1175/JCLI-D-16-0573.1.

Ashok, K., S. K. Behera, S. A. Rao, H. Weng, and T. Yamagata, 2007: El Niño Modoki and its possible teleconnection. *J. Geophys. Res.*, **112**, C11007, https://doi.org/10.1029/2006JC003798.

Bjerknes, J., 1969: Atmospheric teleconnections from the equatorial Pacific. *Mon. Wea. Rev.*, **97**, 163–172, https://doi.org/10.1175/1520-0493(1969)097<0163:ATFTEP>2.3.CO;2.

Bollasina, M. A., and Y. Ming, 2013: The role of land-surface processes in modulating the Indian monsoon annual cycle. *Climate Dyn.*, **41**, 2497–2509–, https://doi.org/10.1007/s00382-012-1634-3.

——, ——, and V. Ramaswamy, 2011: Anthropogenic aerosols and the weakening of the South Asian summer monsoon. *Science*, **334**, 502–505, https://doi.org/10.1126/science.1204994.

Bretherton, C. S., C. Smith, and J. M. Wallace, 1992: An intercomparison of methods for finding coupled patterns in climate data. *J. Climate*, **5**, 541–560, https://doi.org/10.1175/1520-0442(1992)005<0541:AIOMFF>2.0.CO;2.

Cherry, S., 1997: Some comments on singular value decomposition analysis. *J. Climate*, **10**, 1759–1761, https://doi.org/10.1175/1520-0442(1997)010<1759:SCOSVD>2.0.CO;2.

Chinta, V., Z. Chen, Y. Du, and J. S. Chowdary, 2022: Influence of the interdecadal Pacific oscillation on South Asian and East Asian summer monsoon rainfall in CMIP6 models. *Climate Dyn.*, **58**, 1791–1809, https://doi.org/10.1007/s00382-021-05992-6.

Choudhury, B. A., P. V. Rajesh, Y. Zahan, and B. Goswami, 2022: Evolution of the Indian summer monsoon rainfall simulations from CMIP3 to CMIP6 models. *Climate Dyn.*, **58**, 2637–2662, https://doi.org/10.1007/s00382-021-06023-0.

Chowdary, J. S., A. Parekh, and C. Gnanaseelan, 2021: *Indian Summer Monsoon Variability: El Niño–Teleconnections and Beyond*. 1st ed. Elsevier, 472 pp.

Clement, A. C., R. Seager, M. A. Cane, and S. E. Zebiak, 1996: An ocean dynamical thermostat. *J. Climate*, **9**, 2190–2196, https://doi.org/10.1175/1520-0442(1996)009<2190:AODT>2.0.CO;2.

Cleveland, W. S., and S. J. Devlin, 1988: Locally weighted regression: An approach to regression analysis by local fitting. *J. Amer. Stat. Assoc.*, **83**, 596–610, https://doi.org/10.1080/01621459.1988.10478639.

Dai, A., H. Li, Y. Sun, L.-C. Hong, LinHo, C. Chou, and T. Zhou, 2013: The relative roles of upper and lower tropospheric thermal contrasts and tropical influences in driving Asian summer monsoons. *J. Geophys. Res. Atmos.*, **118**, 7024–7045, https://doi.org/10.1002/jgrd.50565.

Dee, D. P., and Coauthors, 2011: The ERA-Interim reanalysis: Configuration and performance of the data assimilation system. *Quart. J. Roy. Meteor. Soc.*, **137**, 553–597, https://doi.org/10.1002/qj.828.

Endo, H., A. Kitoh, and H. Ueda, 2018: A unique feature of the Asian summer monsoon response to global warming: The role of different land–sea thermal contrast change between the lower and upper troposphere. *SOLA*, **14**, 57–63, https://doi.org/10.2151/sola.2018-010.

Eyring, V., S. Bony, G. A. Meehl, C. A. Senior, B. Stevens, R. J. Stouffer, and K. E. Taylor, 2016: Overview of the Coupled Model Intercomparison Project phase 6 (CMIP6) experimental design and organization. *Geosci. Model Dev.*, **9**, 1937–1958, https://doi.org/10.5194/gmd-9-1937-2016.

Farneti, R., A. Stiz, and J. B. Ssebandeke, 2022: Improvements and persistent biases in the southeast tropical Atlantic in CMIP models. *npj Climate Atmos. Sci.*, **5**, 42, https://doi.org/10.1038/s41612-022-00264-4.

Gadgil, S., P. N. Vinayachandran, P. A. Francis, and S. Gadgil, 2004: Extremes of the Indian summer monsoon rainfall, ENSO and equatorial Indian Ocean oscillation. *Geophys. Res. Lett.*, **31**, L12213, https://doi.org/10.1029/2004GL019733.

Ge, F., F. Sielmann, X. Zhu, K. Fraedrich, X. Zhi, T. Peng, and L. Wang, 2017: The link between Tibetan Plateau monsoon and Indian summer precipitation: A linear diagnostic perspective. *Climate Dyn.*, **49**, 4201–4215, https://doi.org/10.1007/s00382-017-3585-1.

Goswami, B. N., V. Krishnamurthy, and H. Annmalai, 1999: A broad-scale circulation index for the interannual variability of the Indian summer monsoon. *Quart. J. Roy. Meteor. Soc.*, **125**, 611–633, https://doi.org/10.1002/qj.49712555412.

Heede, U. K., A. V. Fedorov, and N. J. Burls, 2020: Time scales and mechanisms for the tropical Pacific response to global warming: A tug of war between the ocean thermostat and weaker Walker. *J. Climate*, **33**, 6101–6118, https://doi.org/10.1175/JCLI-D-19-0690.1.

Held, I. M., and B. J. Soden, 2006: Robust responses of the hydrological cycle to global warming. *J. Climate*, **19**, 5686–5699, https://doi.org/10.1175/JCLI3990.1.

Hodges, J. L., 1958: The significance probability of the Smirnov two-sample test. *Ark. Mat.*, **3**, 469–486, https://doi.org/10.1007/BF02589501.

Huang, X., and Coauthors, 2020: The recent decline and recovery of Indian summer monsoon rainfall: Relative roles of external forcing and internal variability. *J. Climate*, **33**, 5035–5060, https://doi.org/10.1175/JCLI-D-19-0833.1.

Hurley, J. V., and W. R. Boos, 2013: Interannual variability of monsoon precipitation and local subcloud equivalent potential temperature. *J. Climate*, **26**, 9507–9527, https://doi.org/10.1175/JCLI-D-12-00229.1.

Jain, S., and V. Kumar, 2012: Trend analysis of rainfall and temperature data for India. *Curr. Sci.*, **102**, 37–49.

——, P. Salunke, S. K. Mishra, and S. Sahany, 2019: Performance of CMIP5 models in the simulation of Indian summer monsoon. *Theor. Appl. Climatol.*, **137**, 1429–1447, https://doi.org/10.1007/s00704-018-2674-3.

Jin, C., B. Wang, and J. Liu, 2020: Future changes and controlling factors of the eight regional monsoons projected by CMIP6 models. *J. Climate*, **33**, 9307–9326, https://doi.org/10.1175/JCLI-D-20-0236.1.

Jin, Q., and C. Wang, 2017: A revival of Indian summer monsoon rainfall since 2002. *Nat. Climate Change*, **7**, 587–594, https://doi.org/10.1038/nclimate3348.

Joshi, M. K., and F. Kucharski, 2017: Impact of interdecadal Pacific oscillation on Indian summer monsoon rainfall: An assessment from CMIP5 climate models. *Climate Dyn.*, **48**, 2375–2391, https://doi.org/10.1007/s00382-016-3210-8.

Katzenberger, A., J. Schewe, J. Pongratz, and A. Levermann, 2021: Robust increase of Indian monsoon rainfall and its variability under future warming in CMIP6 models. *Earth Syst. Dyn.*, **12**, 367–386, https://doi.org/10.5194/esd-12-367-2021.

Lalande, M., M. Ménégoz, G. Krinner, K. Naegeli, and S. Wunderle, 2021: Climate change in the high mountain Asia in CMIP6. *Earth Syst. Dyn.*, **12**, 1061–1098, https://doi.org/10.5194/esd-12-1061-2021.

Lau, W. K.-M., and K.-M. Kim, 2017: Competing influences of greenhouse warming and aerosols on Asian summer monsoon circulation and rainfall. *Asia-Pac. J. Atmos. Sci.*, **53**, 181–194, https://doi.org/10.1007/s13143-017-0033-4.

Levine, R. C., A. G. Turner, D. Marathayil, and G. M. Martin, 2013: The role of northern Arabian Sea surface temperature biases in CMIP5 model simulations and future projections of Indian summer monsoon rainfall. *Climate Dyn.*, **41**, 155–172, https://doi.org/10.1007/s00382-012-1656-x.

Li, G., S.-P. Xie, and Y. Du, 2015: Monsoon-induced biases of climate models over the tropical Indian Ocean. *J. Climate*, **28**, 3058–3072, https://doi.org/10.1175/JCLI-D-14-00740.1.

——, ——, C. He, and Z. Chen, 2017: Western pacific emergent constraint lowers projected increase in Indian summer monsoon rainfall. *Nat. Climate Change*, **7**, 708–712, https://doi.org/10.1038/nclimate3387.

Li, X., M. Ting, and D. E. Lee, 2018: Fast adjustments of the Asian summer monsoon to anthropogenic aerosols. *Geophys. Res. Lett.*, **45**, 1001–1010, https://doi.org/10.1002/2017GL076667.

Li, Z., and Coauthors, 2016: Aerosol and monsoon climate interactions over Asia. *Rev. Geophys.*, **54**, 866–929, https://doi.org/10.1002/2015RG000500.

Lian, T., D. Chen, J. Ying, P. Huang, and Y. Tang, 2018: Tropical Pacific trends under global warming: El Niño–like or La Niña–like? *Natl. Sci. Rev.*, **5**, 810–812, https://doi.org/10.1093/nsr/nwy134.

Lin, M., and P. Huybers, 2019: If rain falls in India and no one reports it, are historical trends in monsoon extremes biased? *Geophys. Res. Lett.*, **46**, 1681–1689, https://doi.org/10.1029/2018GL079709.

Luo, Y., J. Lu, F. Liu, and O. Garuba, 2017: The role of ocean dynamical thermostat in delaying the El Niño–like response over the equatorial Pacific to climate warming. *J. Climate*, **30**, 2811–2827, https://doi.org/10.1175/JCLI-D-16-0454.1.

Ma, J., and J.-Y. Yu, 2014: Paradox in south Asian summer monsoon circulation change: Lower tropospheric strengthening and upper tropospheric weakening. *Geophys. Res. Lett.*, **41**, 2934–2940, https://doi.org/10.1002/2014GL059891.

McGregor, S., M. F. Stuecker, J. B. Kajtar, M. H. England, and M. Collins, 2018: Model tropical Atlantic biases underpin diminished Pacific decadal variability. *Nat. Climate Change*, **8**, 493–498, https://doi.org/10.1038/s41558-018-0163-4.

Ming, Y., V. Ramaswamy, and G. Chen, 2011: A model investigation of aerosol-induced changes in boreal winter extratropical circulation. *J. Climate*, **24**, 6077–6091, https://doi.org/10.1175/2011JCLI4111.1.

Mohapatra, G. N., A. R. Beham, C. Kavyashree, S. Kavya, M. L. Singh, and J. Vaishnavi, 2018: Study of Indian summer monsoon rainfall trend during the period 1901–2013 through data mining. *Int. J. Res. Appl. Sci. Eng. Technol.*, **6**, 1701–1705, https://doi.org/10.22214/ijraset.2018.5278.

Oueslati, B., S. Bony, C. Risi, and J.-L. Dufresne, 2016: Interpreting the inter-model spread in regional precipitation projections in the tropics: Role of surface evaporation and cloud radiative effects. *Climate Dyn.*, **47**, 2801–2815, https://doi.org/10.1007/s00382-016-2998-6.

Parthasarathy, B., A. A. Munot, and D. R. Kothawale, 1994: All-India monthly and seasonal rainfall series: 1871–1993. *Theor. Appl. Climatol.*, **49**, 217–224, https://doi.org/10.1007/BF00867461.

Polson, D., M. Bollasina, G. C. Hegerl, and L. J. Wilcox, 2014: Decreased monsoon precipitation in the Northern Hemisphere due to anthropogenic aerosols. *Geophys. Res. Lett.*, **41**, 6023–6029, https://doi.org/10.1002/2014GL060811.

Prodhomme, C., P. Terray, S. Masson, T. Izumo, T. Tozuka, and T. Yamagata, 2014: Impacts of Indian Ocean SST biases on the Indian monsoon: As simulated in a global coupled model. *Climate Dyn.*, **42**, 271–290, https://doi.org/10.1007/s00382-013-1671-6.

Racherla, P. N., D. T. Shindell, and G. S. Faluvegi, 2012: The added value to global model projections of climate change by dynamical downscaling: A case study over the continental U.S. using the GISS-ModelE2 and WRF models. *J. Geophys. Res.*, **117**, D20118, https://doi.org/10.1029/2012JD018091.

Raghavan, K., and Coauthors, 2016: Deciphering the desiccation trend of the South Asian monsoon hydroclimate in a warming world. *Climate Dyn.*, **47**, 1007–1027, https://doi.org/10.1007/s00382-015-2886-5.

Rajendran, K., S. Surendran, S. J. Varghese, and A. Sathyanath, 2022: Simulation of Indian summer monsoon rainfall, interannual variability and teleconnections: Evaluation of CMIP6 models. *Climate Dyn.*, **58**, 2693–2723, https://doi.org/10.1007/s00382-021-06027-w.

Ramage, C. S., Ed., 1971: Definition of the monsoons and their extent. *Monsoon Meteorology*, International Geophysics Series, Vol. 15, Academic Press, 1–7.

Rao, S. A., and Coauthors, 2019: Monsoon mission: A targeted activity to improve monsoon prediction across scales. *Bull. Amer. Meteor. Soc.*, **100**, 2509–2532, https://doi.org/10.1175/BAMS-D-17-0330.1.

Richter, I., and H. Tokinaga, 2020: An overview of the performance of CMIP6 models in the tropical Atlantic: Mean state, variability, and remote impacts. *Climate Dyn.*, **55**, 2579–2601, https://doi.org/10.1007/s00382-020-05409-w.

Roxy, M. K., 2017: Land warming revives monsoon. *Nat. Climate Change*, **7**, 549–550, https://doi.org/10.1038/nclimate3356.

——, K. Ritika, P. Terray, R. Murtugudde, K. Ashok, and B. N. Goswami, 2015: Drying of Indian subcontinent by rapid Indian Ocean warming and a weakening land–sea thermal gradient. *Nat. Commun.*, **6**, 7423, https://doi.org/10.1038/ncomms8423.

Roy, I., R. G. Tedeschi, and M. Collins, 2019: ENSO teleconnections to the Indian summer monsoon under changing climate. *Int. J. Climatol.*, **39**, 3031–3042, https://doi.org/10.1002/joc.5999.

Sabeerali, C. T., S. A. Rao, A. R. Dhakate, K. Salunke, and B. N. Goswami, 2015: Why ensemble mean projection of South Asian monsoon rainfall by CMIP5 models is not reliable? *Climate Dyn.*, **45**, 161–174, https://doi.org/10.1007/s00382-014-2269-3.

Saha, A., S. Ghosh, A. S. Sahana, and E. P. Rao, 2014: Failure of CMIP5 climate models in simulating post-1950 decreasing trend of Indian monsoon. *Geophys. Res. Lett.*, **41**, 7323–7330, https://doi.org/10.1002/2014GL061573.

Salzmann, M., and R. Cherian, 2015: On the enhancement of the Indian summer monsoon drying by Pacific multidecadal variability during the latter half of the twentieth century. *J. Geophys. Res. Atmos.*, **120**, 9103–9118, https://doi.org/10.1002/2015JD023313.

——, H. Weser, and R. Cherian, 2014: Robust response of Asian summer monsoon to anthropogenic aerosols in CMIP5 models. *J. Geophys. Res. Atmos.*, **119**, 11 321–11 337, https://doi.org/10.1002/2014JD021783.

Seager, R., N. Naik, and G. A. Vecchi, 2010: Thermodynamic and dynamic mechanisms for large-scale changes in the hydrological cycle in response to global warming. *J. Climate*, **23**, 4651–4668, https://doi.org/10.1175/2010JCLI3655.1.

Seth, A., A. Giannini, M. Rojas, S. A. Rauscher, S. Bordoni, D. Singh, and S. J. Camargo, 2019: Monsoon responses to climate changes—connecting past, present and future. *Curr. Climate Change Rep.*, **5**, 63–79, https://doi.org/10.1007/s40641-019-00125-y.

Shamal, M., and J. Sanjay, 2021: An observational equatorial Atlantic Ocean constraint on Indian monsoon precipitation projections. *Climate Dyn.*, **57**, 209–221, https://doi.org/10.1007/s00382-021-05703-1.

Singh, D., S. Ghosh, M. K. Roxy, and S. McDermid, 2019: Indian summer monsoon: Extreme events, historical changes, and role of anthropogenic forcings. *Wiley Interdiscip. Rev. Climate Change*, **10**, e571, https://doi.org/10.1002/wcc.571.

Sooraj, K. P., P. Terray, S. Masson, and J. Crétat, 2019: Modulations of the Indian summer monsoon by the hot subtropical deserts: Insights from coupled sensitivity experiments. *Climate Dyn.*, **52**, 4527–4555, https://doi.org/10.1007/s00382-018-4396-8.

Sperber, K. R., H. Annamalai, I.-S. Kang, A. Kitoh, A. Moise, A. Turner, B. Wang, and T. Zhou, 2013: The Asian summer monsoon: An intercomparison of CMIP5 vs. CMIP3 simulations of the late 20th century. *Climate Dyn.*, **41**, 2711–2744, https://doi.org/10.1007/s00382-012-1607-6.

Swapna, P., R. Krishnan, N. Sandeep, A. G. Prajeesh, D. C. Ayantika, S. Manmeet, and R. Vellore, 2018: Long-term climate simulations using the IITM Earth System Model (IITM-ESMv2) with focus on the South Asian monsoon. *J. Adv. Model. Earth Syst.*, **10**, 1127–1149, https://doi.org/10.1029/2017MS001262.

Tanaka, H. L., N. Ishizaki, and A. Kitoh, 2004: Trend and interannual variability of Walker, monsoon and Hadley circulations defined by velocity potential in the upper troposphere. *Tellus*, **56A**, 250–269, https://doi.org/10.3402/tellusa.v56i3.14410.

Terray, P., K. P. Sooraj, S. Masson, R. P. M. Krishna, G. Samson, and A. G. Prajeesh, 2018: Towards a realistic simulation of boreal summer tropical rainfall climatology in state-of-the-art coupled models: Role of the background snow-free land albedo. *Climate Dyn.*, **50**, 3413–3439, https://doi.org/10.1007/s00382-017-3812-9.

——, ——, ——, and C. Prodhomme, 2021: Anatomy of the Indian summer monsoon and ENSO relationships in state-of-the-art CGCMs: Role of the tropical Indian Ocean. *Climate Dyn.*, **56**, 329–356, https://doi.org/10.1007/s00382-020-05484-z.

——, L. Joseph, and K. Sooraj, 2023: Anatomy of the Indian summer monsoon and ENSO relationship in a state-of-the-art CGCM: Role of the tropical Atlantic Ocean. *Climate Dyn.*, **60**, 1559–1582, https://doi.org/10.1007/s00382-022-06397-9.

Tian, B., and X. Dong, 2020: The double-ITCZ bias in CMIP3, CMIP5, and CMIP6 models based on annual mean precipitation. *Geophys. Res. Lett.*, **47**, e2020GL087232, https://doi.org/10.1029/2020GL087232.

Vecchi, G. A., and B. J. Soden, 2007: Global warming and the weakening of the tropical circulation. *J. Climate*, **20**, 4316–4340, https://doi.org/10.1175/JCLI4258.1.

Vibhute, A., S. Halder, P. Singh, A. Parekh, J. S. Chowdary, and C. Gnanaseelan, 2020: Decadal variability of tropical Indian Ocean sea surface temperature and its impact on the Indian summer monsoon. *Theor. Appl. Climatol.*, **141**, 551–566, https://doi.org/10.1007/s00704-020-03216-1.

Wang, B., C. Jin, and J. Liu, 2020: Understanding future change of global monsoons projected by CMIP6 models. *J. Climate*, **33**, 6471–6489, https://doi.org/10.1175/JCLI-D-19-0993.1.

Wang, M., and Coauthors, 2015: A multiscale modeling framework model (superparameterized CAM5) with a higher-order turbulence closure: Model description and low-cloud simulations. *J. Adv. Model. Earth Syst.*, **7**, 484–509, https://doi.org/10.1002/2014MS000375.

Watanabe, M., J.-L. Dufresne, Y. Kosaka, T. Mauritsen, and H. Tatebe, 2021: Enhanced warming constrained by past trends in equatorial Pacific sea surface temperature gradient. *Nat. Climate Change*, **11**, 33–37, https://doi.org/10.1038/s41558-020-00933-3.

Webster, P. J., and S. Yang, 1992: Monsoon and ENSO: Selectively interactive systems. *Quart. J. Roy. Meteor. Soc.*, **118**, 877–926, https://doi.org/10.1002/qj.49711850705.

Wilcox, L. J., E. J. Highwood, and N. J. Dunstone, 2013: The influence of anthropogenic aerosol on multi-decadal variations of historical global climate. *Environ. Res. Lett.*, **8**, 024033, https://doi.org/10.1088/1748-9326/8/2/024033.

Zhou, T., and Coauthors, 2016: GMMIP (v1.0) contribution to CMIP6: Global monsoons model inter-comparison project. *Geosci. Model Dev.*, **9**, 3589–3604, https://doi.org/10.5194/gmd-9-3589-2016.